SCIENCE CHINA
Technological Sciences

•Article•

January 2022 Vol.65 No.1: 115–130
https://doi.org/10.1007/s11431-020-1894-y

Ramping loss and mechanical response in a no-insulation high-temperature superconducting layer-wound coil and intra-layers no-insulation coil

LI DongKe[1,2], LIU DongHui[1,2] & YONG HuaDong[1,2*]

[1] *Key Laboratory of Mechanics on Disaster and Environment in Western China, Ministry of Education of China, Lanzhou University, Lanzhou 730000, China;*
[2] *Department of Mechanics and Engineering Sciences, College of Civil Engineering and Mechanics, Lanzhou University, Lanzhou 730000, China*

Received December 25, 2020; accepted July 13, 2021; published online November 3, 2021

The layer-wound coil has a great potential in nuclear magnetic resonance and magnetic resonance imaging owing to the better spatial homogeneity of the magnetic field. However, high-temperature superconducting (HTS) coil wound by no-insulation (NI) layer-wound technique has been verified with a long field delay time. A new method named the intra-layer no-insulation (LNI) winding technique has been proposed to reduce the charging delay time of the coil. This paper is mainly to study and compare the ramping loss and mechanical characteristics of the layer-wound coil and LNI coil. The results indicate that the total ramping loss can be significantly reduced by using the LNI winding method. The effects of the ramping rate of power supply current and the contact resistivity on the ramping loss are also discussed in the paper. Furthermore, the stress distributions in the layer-wound coil and LNI coil are compared, where the cooling process and Lorentz force are both considered. It can be found that the copper sheet of the LNI coil experiences relatively higher stress than its (RE)$Ba_2Cu_3O_x$ (REBCO) conductor layer. Meanwhile, the magnitude of stress generated in the REBCO conductor of the LNI coil is slightly different from that of the layer-wound coil.

high-temperature superconducting coil, ramping loss, stress

Citation: Li D K, Liu D H, Yong H D. Ramping loss and mechanical response in a no-insulation high-temperature superconducting layer-wound coil and intra-layers no-insulation coil. Sci China Tech Sci, 2022, 65: 115–130, https://doi.org/10.1007/s11431-020-1894-y

1 Introduction

The no-insulation (NI) high-temperature superconducting (HTS) coil is wound directly without turn-to-turn electrical insulation [1]. When a local quench occurs, the current of the NI coil can bypass local hotspots due to low contact resistance [2–5]. Namely, this characteristic drastically reduces the Joule heating generated in the coil during the thermal runaway, which prevents local overheating and damage [6,7]. Thus, the NI coil has a self-protecting feature during the local quench [8–11]. However, the current can also flow along the radial direction of the coil through low contact resistance during charging and discharging, which leads to a long magnetic field delay time [1,12–14].

In comparison to the NI pancake-wound coil, the NI layer-wound coil has a longer magnetic field delay time, which has been validated in previous publications [15,16]. However, the layer-wound coil can provide better spatial homogeneity of the magnetic field, which is popular in nuclear magnetic resonance (NMR) and magnetic resonance imaging (MRI) [16–19]. To mitigate long magnetic field delay time, a new winding method has been proposed, named ‘intra-layer no-insulation (LNI)’ coil [20,21]. Specifically, a polyimide sheet and a copper sheet are both inserted between different layers

*Corresponding author (email: yonghd@lzu.edu.cn)

of the layer-wound coil. The experimental results indicate that not only can LNI coil reduce the magnetic field delay time, but also has high thermal stability [22].

In the charging process, the ramping loss of the NI coil mainly includes two parts: the magnetization loss induced by flux creep in the superconducting layer [23–27] and contact loss generated by radial current between turns [28]. For large-scale NI magnets, the ramping process of the power supply current is usually interrupted several times because of the temperature rise induced by ramping loss [29]. Furthermore, there are more and more concerns about the mechanical damage of HTS magnets [30–34]. The delamination has been observed in superconductor tapes after the quench of the magnet [35]. Moreover, large hoop stress is generated by the prestress and strong electromagnetic force in a high magnetic field, which may affect the critical current of the coils [36,37]. The supporting structure might be damaged because of a large unbalanced axial force in the magnet [38,39]. Therefore, it is meaningful to clearly understand the distributions of the loss and stress in order to operate NI magnets safely.

This paper is mainly to analyze and compare the ramping loss and mechanical behaviors of the layer-wound coil and LNI coil. An equivalent axisymmetrical circuit model combined with a T-A formulation is built to calculate the ramping loss. The mechanical behaviors of the coils are analyzed with a homogeneous mechanical model. The descriptions of the numerical model are given in Sect. 2. Sect. 3 discusses the ramping loss and the effects of two factors. In Sect. 4, the distributions of stress in the coils are shown in three different cases. The conclusions are summarized in Sect. 5.

2 Numerical model

In the following part, two different coils are investigated in the simulation. One is a forty-layer and ten-turn NI layer-wound coil, and the other is an LNI coil. Figure 1(a) and (c) show the cross section and equivalent circuit for the layer-wound coil, respectively. The corresponding diagrams of the LNI coil are shown in Figure 1(b) and (d). Meanwhile, the serial number of each turn is defined according to the di-

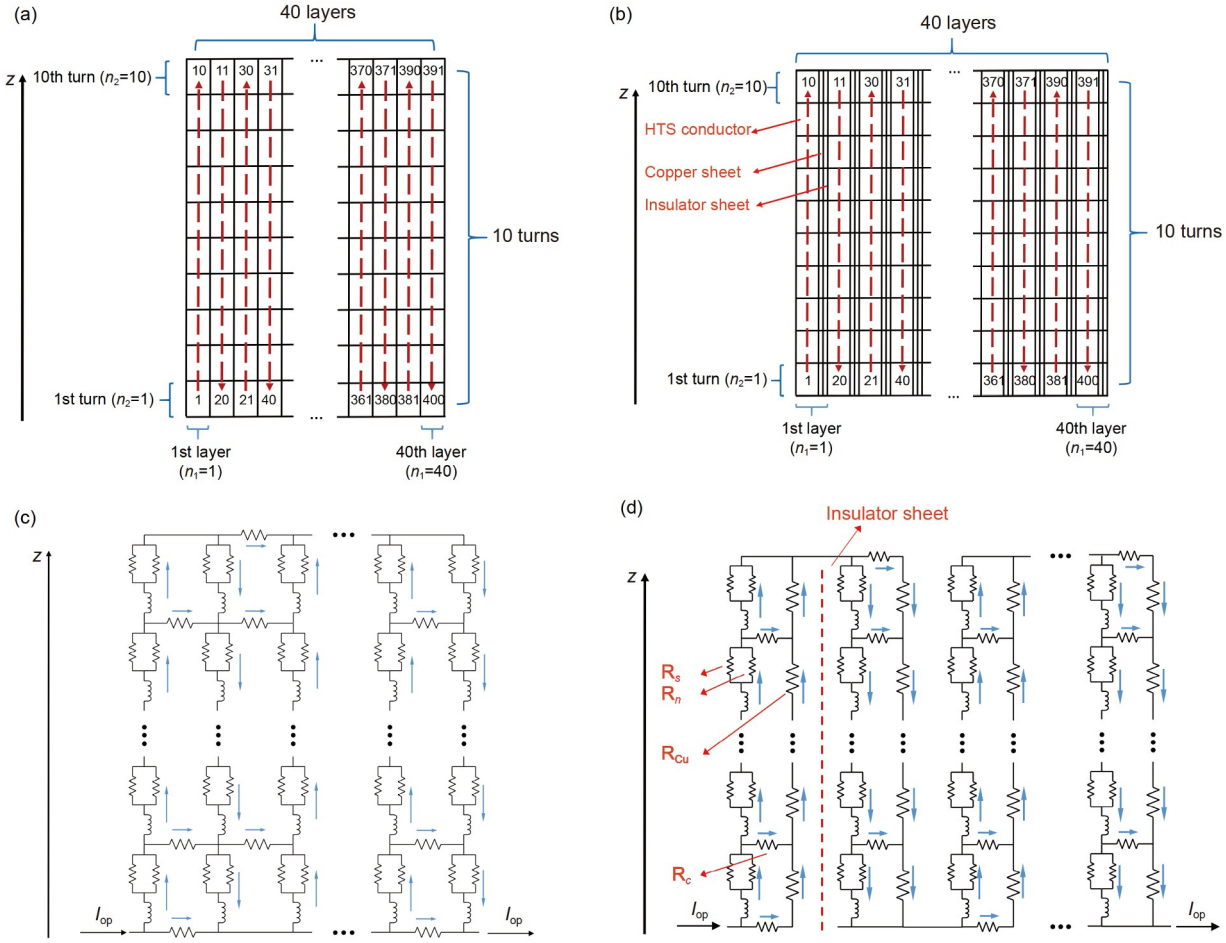

Figure 1 (Color online) (a), (b) The schematic of an NI layer-wound coil and LNI coil; (c), (d) the equivalent circuit model for an NI layer-wound coil and LNI coil.

rection of the transport current. In the simulation, $n_1(1 \le n_1 \le 40)$ is defined as the number of layers from the innermost layer to the outermost layer of the coil, and $n_2(1 \le n_2 \le 10)$ is defined as the number of turns from the bottom to the top of the coil. In the simulation, the coils are wound by (RE)$Ba_2Cu_3O_x$ (REBCO) tapes, where the parameters are given in the ref. [40]. The detailed parameters about the coils and the REBCO tapes are shown in Table 1 [20,40,41].

2.1 Equivalent circuit model

The current in each turn is calculated by an equivalent axisymmetrical circuit model [16,20,40,42], as shown in Figure 1(c) and (d). For the layer-wound coil, the current of each turn can flow into adjacent turns through the contact surface. The governing equation can be derived from Kirchhoff's voltage law at each independent circuit mesh, which can be expressed as follows:

$$\begin{cases} \sum_{k=1}^{400}\left(M_{1,k}\dfrac{\mathrm{d}i_k}{\mathrm{d}t}+M_{20,k}\dfrac{\mathrm{d}i_k}{\mathrm{d}t}\right)+\left(V_{\mathrm{sc},1}+V_{\mathrm{sc},20}\right) \\ \quad +\left(R_{r,2}i_{r,2}-R_{r,1}i_{r,1}\right)=0, \\ \sum_{k=1}^{400}\left(M_{2,k}\dfrac{\mathrm{d}i_k}{\mathrm{d}t}+M_{19,k}\dfrac{\mathrm{d}i_k}{\mathrm{d}t}\right)+\left(V_{\mathrm{sc},2}+V_{\mathrm{sc},19}\right) \\ \quad +\left(R_{r,3}i_{r,3}-R_{r,2}i_{r,2}\right)=0, \\ \quad \vdots \\ \sum_{k=1}^{400}\left(M_{390,k}\dfrac{\mathrm{d}i_k}{\mathrm{d}t}+M_{391,k}\dfrac{\mathrm{d}i_k}{\mathrm{d}t}\right)+\left(V_{\mathrm{sc},390}+V_{\mathrm{sc},391}\right) \\ \quad -R_{r,390}i_{r,390}=0, \end{cases} \tag{1}$$

where $M_{j,k}$ is the self inductance $(j=k)$ and mutual inductance $(j \ne k)$ between the jth and kth turns of the coil. $V_{\mathrm{sc},k}$ represents the voltage of the superconductor layer. i_k and $i_{r,j}$ represent the circumferential current and the radial current in each turn, respectively. The subscript k $(1 \le k \le 400)$ and j $(1 \le j \le 390)$ both represent the turn number. $R_{r,j}$ represents the contact resistance, which can be calculated as

$$R_{r,j}=\frac{\rho_r}{S_j}, \tag{2}$$

where ρ_r and S_j are the contact resistivity and the surface area of the jth turn. The typical value of contact resistivity is 70 μΩ cm^2 [41]. The radial current $i_{r,j}$ can be calculated by the power supply current and circumferential current. The self and mutual inductances are calculated on the basis of the Neumann formula as follows [43]:

$$M_{j,k}=\frac{\mu_0 r_j r_k}{4\pi w^2} \times \int_{h_k}^{h_k+w}\int_0^{2\pi}\int_{h_j}^{h_j+w}\int_0^{2\pi}\frac{\cos(\theta-\Theta)}{\sqrt{r_j^2+r_k^2-2r_jr_k\cos(\theta-\Theta)+(z-Z)^2+\mathrm{eps}}} \times \mathrm{d}\theta\mathrm{d}z\mathrm{d}\Theta\mathrm{d}Z, \tag{3}$$

where θ, Θ, z, and Z are the positional variables related to the intersection angle and the width of each turn. w is the width of HTS tape. r_j and r_k represent the distances from the central axis of the coil to jth and kth turns, respectively. h_j and h_k are the height of jth and kth turns, respectively. A small amount (eps = 1×10^{-10}) is added to the calculation to avoid the singularity when calculating the self inductance $(j=k)$.

For the LNI coil, although adjacent turns are insulated by a polyimide sheet, the current can flow into the copper sheet through the contact surface. Therefore, the governing equation according to Kirchhoff's voltage law can be expressed as follows:

$$\begin{cases} \sum_{k=1}^{400}M_{1,k}\dfrac{\mathrm{d}i_k}{\mathrm{d}t}+V_{\mathrm{sc},1}+\left(R_{r,2}i_{r,2}-R_{r,1}i_{r,1}\right)-i_{\mathrm{Cu},1}R_{\mathrm{Cu},1}=0, \\ \sum_{k=1}^{400}M_{2,k}\dfrac{\mathrm{d}i_k}{\mathrm{d}t}+V_{\mathrm{sc},2}+\left(R_{r,3}i_{r,3}-R_{r,2}i_{r,2}\right)-i_{\mathrm{Cu},2}R_{\mathrm{Cu},2}=0, \\ \quad \vdots \\ \sum_{k=1}^{400}M_{400,k}\dfrac{\mathrm{d}i_k}{\mathrm{d}t}+V_{\mathrm{sc},400}-R_{r,400}i_{r,400}-i_{\mathrm{Cu},400}R_{\mathrm{Cu},400}=0, \end{cases} \tag{4}$$

where $i_{\mathrm{Cu},k}$ and $R_{\mathrm{Cu},k}$ represent the current and the resistance of the copper sheet of each turn, respectively. Here, it is assumed that the current of the copper sheet mainly flows

Table 1 Specifications of magnets

Parameters	layer-wound coil	LNI coil
Tape width (mm)	4 [40]	4
Tape thickness (mm)	0.2 [40]	0.2
Inserted materials between layers	–	Polyimide sheet (12.5 μm thick)/copper sheet (7 μm thick) [20]
Contact resistivity (μΩ cm^2)	70 [41]	25000 [20]
Inner and outer diameters (mm)	100, 116	100, 117.56
Number of turns	400 (10 turns×40 layers)	400 (10 turns×40 layers)
Height of the magnet (mm)	40	40
Total length (m)	130.69	131.18
Inductance, L_{coil}(mH)	18.8	18.9
I_c magnet, @20K (A)	390	390

along the axial direction, and the effect of mutual inductance between the superconductor layer and the copper sheet is neglected.

In addition, the voltage of the superconductor layer can be calculated as

$$\begin{cases} V_{\mathrm{sc},k} - V_{n,k} = 0, \\ i_k = i_{\mathrm{sc},k} + i_{n,k}, \\ V_{\mathrm{sc},k} = E_c l_k \left(\dfrac{i_{\mathrm{sc},k}}{I_{c,k}} \right)^n, \\ V_{n,k} = i_{n,k} R_{n,k}, \end{cases} \tag{5}$$

where $V_{n,k}$, $i_{n,k}$, and $R_{n,k}$ are the voltage, current, and resistance of the normal layers, respectively. $i_{\mathrm{sc},k}$ is the current of the superconductor layer. The *E-I* power law is used for describing the electrical characteristics of the superconductor layer [44]. Critical electrical field E_c and n value are taken as 1×10^{-4} V/m and 31 [5], respectively. $I_{c,k}$ is the critical current in a magnetic field, which can be calculated as [45]

$$I_{c,k} = \frac{I_{c0}}{\left(1 + \sqrt{(kB_{\parallel})^2 + B_{\perp}^2} / B_c\right)^b}, \tag{6}$$

where $B_{\parallel}$ and $B_{\perp}$ are the magnetic fields parallel and perpendicular to the tape surface, respectively. I_{c0} is 768.45 A, which represents the critical current of the tape at the environment temperature of 20 K [40]. The parameters k, b, and B_c are 0.063, 1.46, and 4.14, respectively [40].

The contact loss power and energy generated by the radial current can be calculated by [40]

$$\begin{cases} W_r = \sum_k i_{r,k}^2 R_{r,k}, \\ Q_r = \int W_r \mathrm{d}t, \end{cases} \tag{7}$$

where W_r and Q_r are contact loss power and energy, respectively.

2.2 T-A formulation

T-A formulation is used with the above equivalent axisymmetrical circuit model to calculate electromagnetic characteristics of superconducting coils [46,47]. The calculations can be implemented with commercial finite element method (FEM) software COMSOL. For the two-dimensional problem, the superconducting layer is approximated as a line structure according to the thin strip approximation. The governing equation of T-A formulation can be expressed as [46,47]

$$\begin{cases} \mathbf{J} = \nabla \times \mathbf{T}, \\ \nabla \times (\rho \nabla \times \mathbf{T}) = -\dfrac{\partial \mathbf{B}}{\partial t}, \\ \nabla \times \left(\dfrac{1}{\mu} \nabla \times \mathbf{A} \right) = \mathbf{J}, \\ \mathbf{B} = \nabla \times \mathbf{A}, \end{cases} \tag{8}$$

where **J**, **T**, **B**, and **A** are the current density vector, current vector potential, magnetic flux density vector, and the magnetic vector potential, respectively. ρ and μ are the resistivity and the magnetic permeability.

Besides, the magnetization loss power W_{sc} and energy Q_{sc} in superconducting layers can be calculated as [40]

$$\begin{cases} W_{\mathrm{sc}} = \int_{\Omega} \mathbf{E} \cdot \mathbf{J} \mathrm{d}\Omega, \\ Q_{\mathrm{sc}} = \int W_{\mathrm{sc}} \mathrm{d}t. \end{cases} \tag{9}$$

2.3 Mechanical model

The two-dimensional axisymmetric homogenous mechanical models for two coils are also built to calculate and compare their mechanical behaviors. In order to reduce the calculation, the REBCO tapes are simplified as an equivalent anisotropic homogeneous material. During the operation, the coil will experience the cooling process. In addition, the coil is also subjected to the Lorentz force. Thus, the effects of thermal strain induced by the cooling process and the Lorentz force on the mechanical deformation of the coil should be taken into account in the simulation. The skeleton and overband of the magnet are not taken into account in this paper. In order to avoid the rigid displacement along the axial direction, it is assumed that the bottom of the coil cannot move along the axial direction, and thus the axial displacement of the bottom boundary is fixed in the simulation. The upper boundary of the coil is assumed to be free because of the coil being in compression along with the height during the cooling and charging. Due to the self-supporting turn effect, the inner and outer boundaries of the coil are chosen to be free [39,48,49]. Since the number of layers along the radial direction is relatively less, the prestress during the winding is lower and neglected in the simulation. The mechanical governing equations are calculated as [50,51]

$$\begin{cases} \tilde{\rho} \dfrac{\partial^2 u}{\partial t^2} = \dfrac{\partial \sigma_r}{\partial r} + \dfrac{\partial \tau_{zr}}{\partial z} + \dfrac{\sigma_r - \sigma_\varphi}{r} + f_r, \\ \tilde{\rho} \dfrac{\partial^2 w}{\partial t^2} = \dfrac{\partial \sigma_z}{\partial z} + \dfrac{\partial \tau_{rz}}{\partial r} + \dfrac{\tau_{rz}}{r} + f_z, \end{cases} \tag{10}$$

$$\varepsilon_r = \frac{\partial u}{\partial r},\ \varepsilon_\varphi = \frac{u}{r},\ \varepsilon_z = \frac{\partial w}{\partial z},\ \gamma_{zr} = \frac{\partial u}{\partial z} + \frac{\partial w}{\partial r}, \tag{11}$$

where $\tilde{\rho}$ is the density, u and w represent radial and axial displacements. The subscripts r, φ, and z represent radial, circumferential, and axial directions, respectively. f_r and f_z are the radial and axial components of the Lorentz force, which can be expressed as follows:

$$f_r = J_\varphi B_z, \quad f_z = -J_\varphi B_r. \tag{12}$$

The constitutive relations in the cylindrical coordinate system can be expressed as

$$\begin{cases} \varepsilon_r = \dfrac{\sigma_r}{E_r} - \upsilon_{\varphi r}\dfrac{\sigma_\varphi}{E_\varphi} - \upsilon_{zr}\dfrac{\sigma_z}{E_z} + \varepsilon_r^{\text{th}}, \\ \varepsilon_\varphi = -\upsilon_{r\varphi}\dfrac{\sigma_r}{E_r} + \dfrac{\sigma_\varphi}{E_\varphi} - \upsilon_{z\varphi}\dfrac{\sigma_z}{E_z} + \varepsilon_\varphi^{\text{th}}, \\ \varepsilon_z = -\upsilon_{rz}\dfrac{\sigma_r}{E_r} - \upsilon_{\varphi z}\dfrac{\sigma_\varphi}{E_\varphi} + \dfrac{1}{E_z} + \varepsilon_z^{\text{th}}, \\ \gamma_{\varphi z} = \dfrac{\tau_{\varphi z}}{G_{\varphi z}},\ \gamma_{zr} = \dfrac{\tau_{zr}}{G_{zr}},\ \gamma_{r\varphi} = \dfrac{\tau_{r\varphi}}{G_{r\varphi}}, \end{cases} \tag{13}$$

in which υ, E, and G are Poisson's ratio, Young's modulus, and shear modulus, respectively. The thermal strain induced by temperature variation during the cooling process can be expressed as

$$\varepsilon^{\text{th}} = \int_{T_0}^{T} \alpha \mathrm{d}T, \tag{14}$$

where α and T_0 are the coefficient of thermal expansion and initial temperature of the coils. The equivalent elastic modulus, Poisson's ratio, and thermal expansion coefficient can be estimated by the homogenization method [52]. Detailed mechanical parameters for different conductor materials are shown in Tables 2 [53–62] and 3 . Note that the mechanical equations are also solved by commercial FEM software COMSOL.

Table 2 Material parameters of different constituent materials [53–62]

	Young's modulus E (GPa)	Poisson's ratio v	CTE α ($\times 10^{-6}$ K^{-1})
Copper	85	0.34	17.7
Hastelloy	175	0.307	14
Silver	76	0.37	17.1
REBCO	157	0.3	11
Buffer	170	0.226	9.5
Polyimide	3	0.34	20

Table 3 Equivalent mechanical parameters

Parameters	Value
E_r; E_φ; E_z (GPa)	121; 131; 131
$G_{r\varphi}$; $G_{\varphi z}$; G_{rz} (GPa)	43; 50; 43
$v_{r\varphi}$; $v_{\varphi z}$; v_{rz}	0.318; 0.302; 0.318
α_r; α_φ; α_z ($\times 10^{-6}$ K^{-1})	16.6; 15.2; 15.2

3 Numerical analysis of ramping loss

The numerical model of the layer-wound coil has been validated in previous publications [16]. The central magnetic field and the supply current of an LNI coil tested by the experiment [20] are compared to the results of numerical simulation in Figure 2. Here, the contact resistivity is 25 mΩ cm^2 according to ref. [20]. It can be found that the computational results are in agreement with the experimental results, and the magnetic field delay time constants are both 0.1 s. Therefore, the numerical model of the LNI coil is effective to estimate its ramping loss.

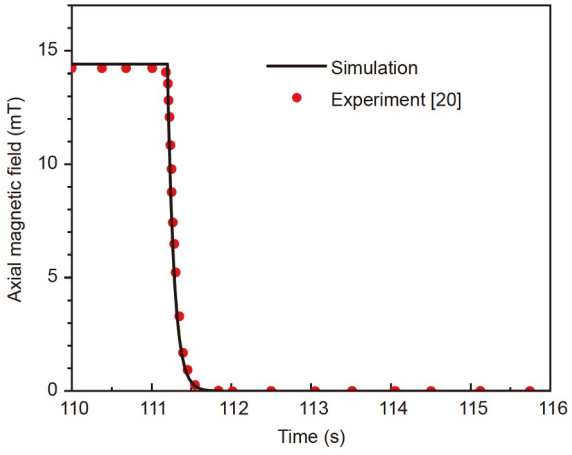

Figure 2 (Color online) The comparisons of the central field from the experiment and simulation.

3.1 The ramping loss power in the coils

In this subsection, the layer-wound coil and the LNI coil are both ramped up to 200 A at a ramping rate of 5 A/s, and holds the current constant (t>40 s). The operating current of the coil is 51% of the critical current (390 A), and thus the exponential loss is ignored. Figure 3 shows the distributions of the circumferential current density, radial current density, and current density in the copper sheet at 40 s. It can be found that the LNI coil has a larger circumferential current and penetration zone than the layer wound coil. In each coil, the bottom and top turns have a more penetration zone than others, which is dependent on the distribution of the magnetic field. The magnetic field perpendicular to the tape surface at the top and bottom turns is higher than that at other turns. Therefore, the coils at both ends have lower critical current owing to the anisotropy of the critical current, which leads to a deeper flux penetration. Moreover, it can be found that the radial current of the LNI coil is reduced compared to the layer wound coil. The distribution of radial current and current in copper sheet is staggered in different layers. In odd layers, the bottom turns have a higher current than the top turns. However, the current distribution shows an opposite trend in even layers.

Figure 4 gives the profiles of the total magnetization loss power of the layer-wound coil and the LNI coil in the charging process. It can be found that the magnetization loss power of the layer-wound coil continues to increase (t>40 s), even if the power supply current reaches a stable state, as shown in Figure 4(a). The reason is that a number of inner turns in the layer-wound coil have a much smaller circumferential current than the power supply current due to a

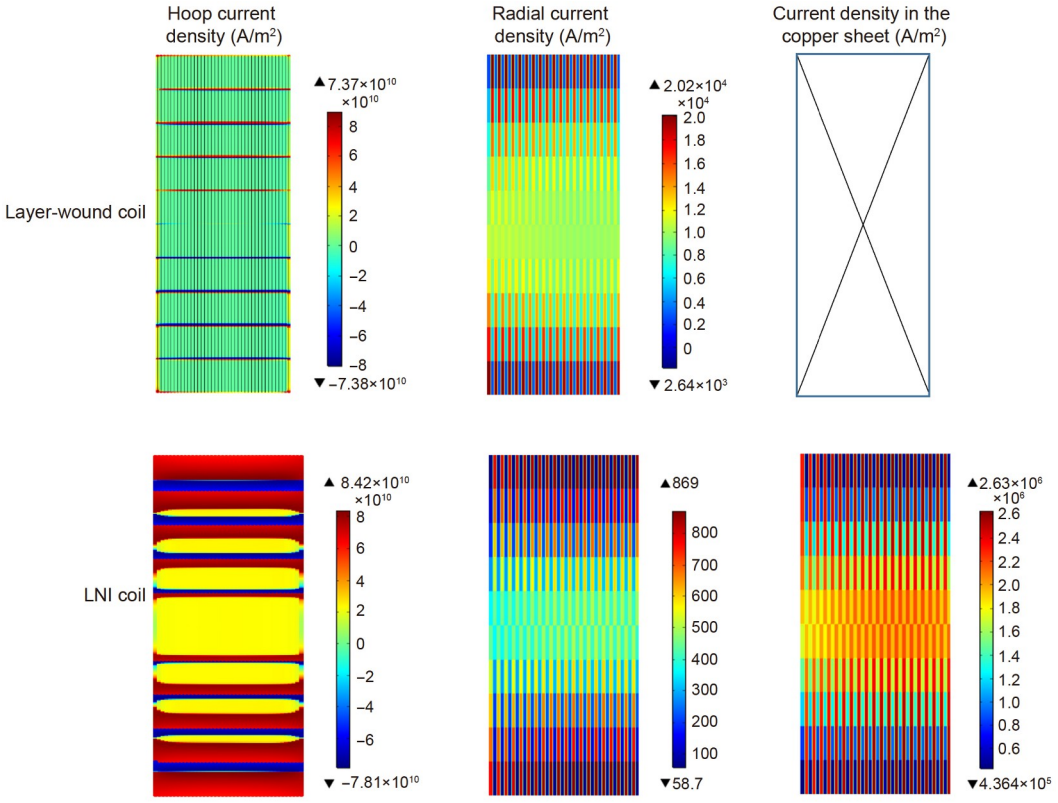

Figure 3 (Color online) The distributions of the circumferential and radial current densities in the coil and current density in the copper sheet at 40 s. Note that the layer-wound coil has no copper sheet.

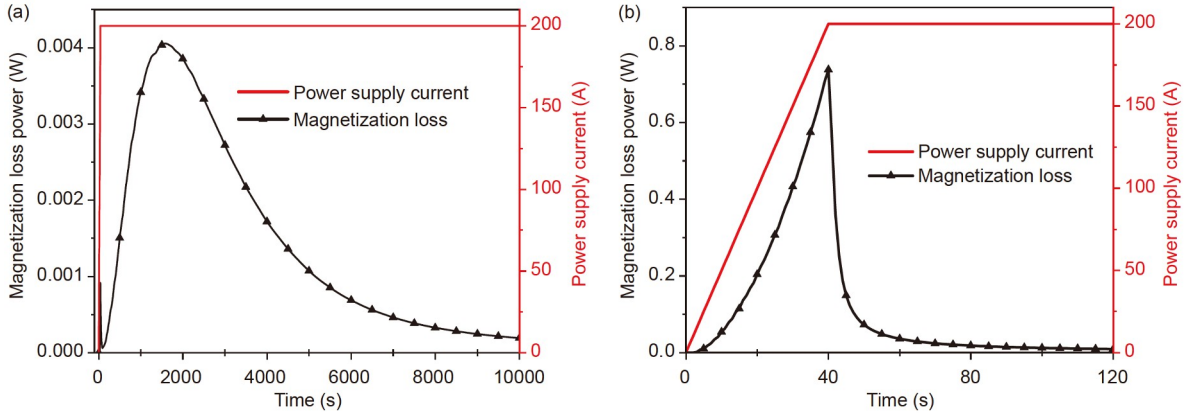

Figure 4 (Color online) The profiles of transport current and magnetization loss power in the ramping process. (a) Layer-wound coil; (b) LNI coil.

strong electromagnetic shielding effect [16]. At t=1600 s, most of the radial currents have transformed into the circumferential currents, and the magnetization loss power of the layer-wound coil starts to decrease. However, the magnetization loss power of the LNI coil reaches the peak value at 40 s, and then decreases rapidly (see Figure 4(b)). Moreover, due to the short charging delay time of the LNI coil, its magnetization loss power also needs less time to reach zero by comparing to the layer-wound coil.

Figure 5 shows the profiles of the contact loss power of the layer-wound coil, the contact loss power, and the copper sheet loss power of the LNI coil. The contact loss power of the layer-wound coil reaches the peak value at 40 s, and then decreases slowly and drops to zero at about 3500 s. The reason is that the inner turns in the layer-wound coil have the largest radial current at 40 s, and thus the contact loss power reaches the peak value. Afterward, the radial current needs much time to transform into the circumferential current in the layer-wound coil, so that the contact loss power decreases slowly and drops to zero at about 3500 s. Although the

contact loss power of the LNI coil has a changing trend similar to the layer-wound coil, it can reduce to zero in a short time. Besides, the transporting current in the LNI coil can flow into the copper sheet, which could lead to copper sheet loss. It can be seen that copper sheet loss power has a similar trend compared with its contact loss power in the LNI coil. Overall, compared with the magnetization loss power in Figure 4, the contact loss power of the layer-wound coil has the main contribution to its total loss power. In the LNI coil, the copper sheet loss power is much lower than the contact loss and magnetization loss power.

3.2 The ramping loss energy in the coils

The sum of the loss energy of all turns in each layer of the two coils is shown in Figure 6. The loss energy shows non-uniform distribution along the radial direction in the whole ramping process. The results indicate that the layers located in the outer side and inner side of the coils have higher magnetization loss energy than other layers (see Figure 6(a)). Because the innermost and outermost layers of the coils have large circumferential current, magnetic flux penetration of these layers is deeper than other layers. As for the contact loss energy, due to the large radial current generated in the outer side of the coils, the turns in these zones have larger contact loss energy in the ramping process for the layer-wound coil (see Figure 6(b)).

Figure 7 shows the sum of the loss energy of all layers in each turn of the two coils. The magnetization loss energy of the two coils shows a similar distribution trend. Meanwhile, the magnetization loss energy generated in top and bottom turns (n_2=1 and n_2=10) is about 57% of the total magnetization loss energy. These results are corresponding with the penetration zone distribution in Figure 3.

Moreover, the turns in the upper and lower sides of the coil have large radial current, and thus the contact loss energy of both coils is higher in their top and bottom turns. However, the copper sheet loss of the LNI coil shows an opposite

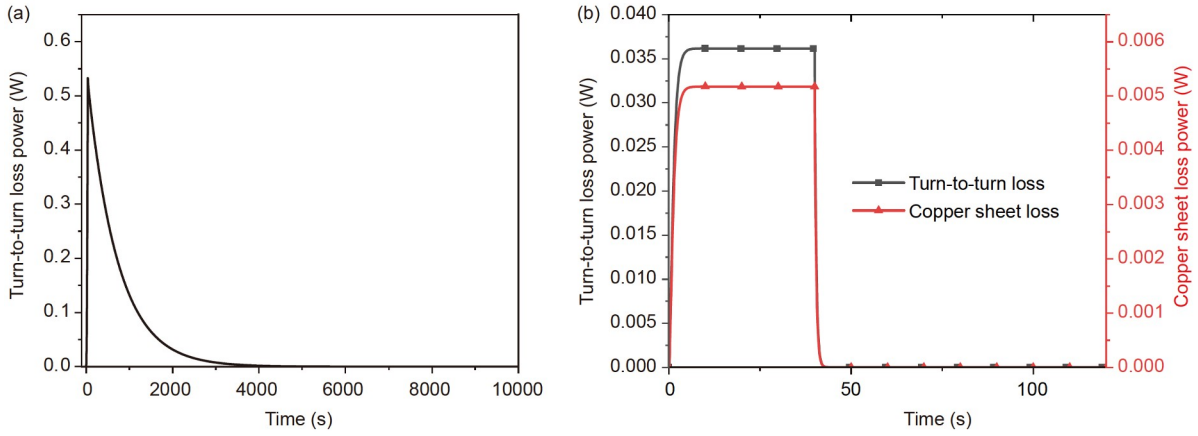

Figure 5 (Color online) (a) The contact loss power of layer-wound coil; (b) the contact loss power and the copper sheet loss power of LNI coil.

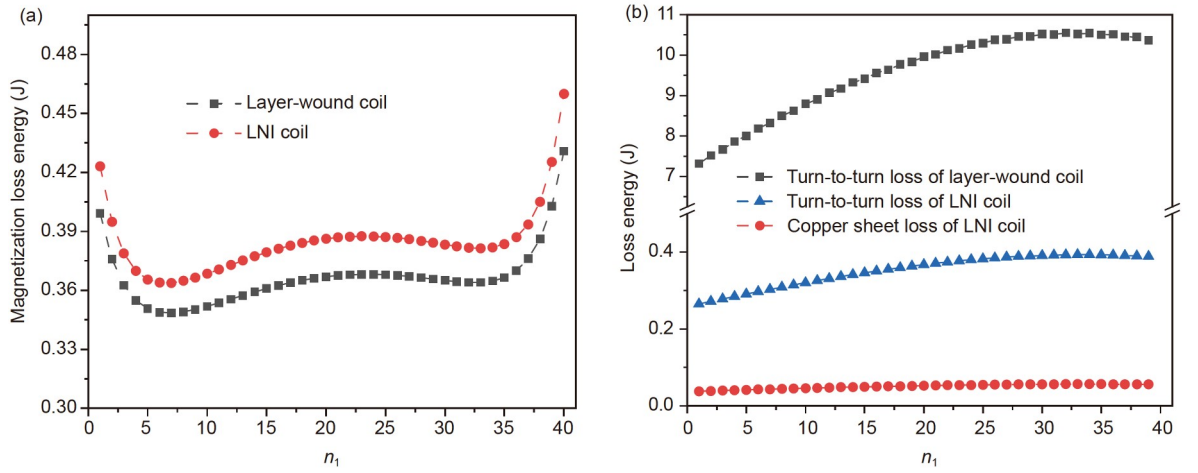

Figure 6 (Color online) The distributions of loss energy along the radial direction of the coils in the ramping process. (a) Magnetization loss energy; (b) contact loss energy and copper sheet loss energy.

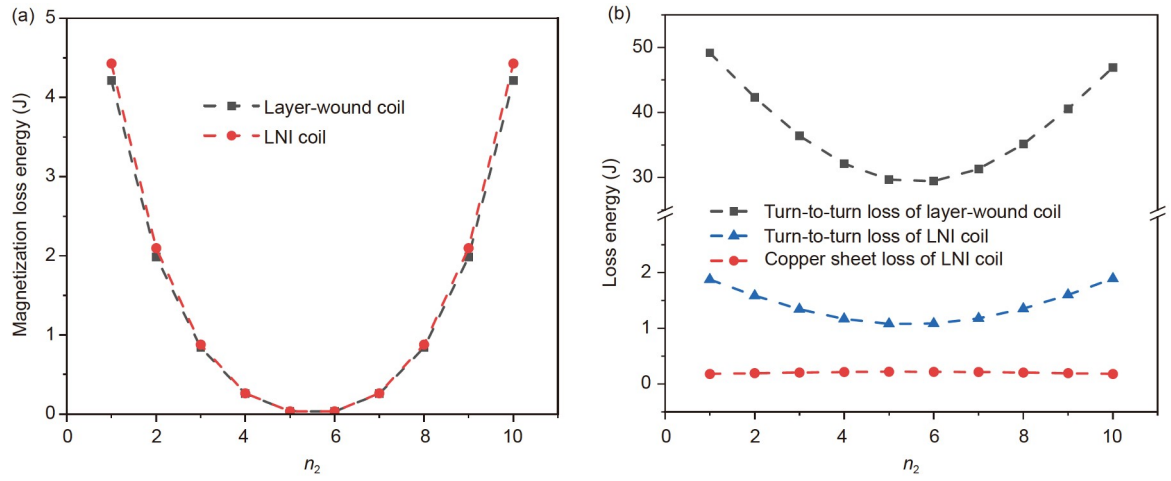

Figure 7 (Color online) The distributions of loss energy along the axial direction of the coils in the ramping process. (a) Magnetization loss energy; (b) contact loss energy and copper sheet loss energy.

distribution. The highest copper sheet loss is generated at the middle turns of the coil. Figure 8 shows the total loss energy in the two coils. It can be found that the total loss energy of the LNI coil increases more rapidly than the layer-wound coil due to a short charging delay time. One key result is that the total loss energy of the layer-wound coil is about ten times of the LNI coil in the whole charging process. Therefore, the LNI coil has a high thermal stability margin in the ramping process.

3.3 The effects of contact resistivity and ramping rate

Figure 9 shows the effect of different contact resistivities from 70 to 25000 μΩ cm^2 on the loss energy of the layer-wound coil and LNI coil. With the increase of contact resistivity, the magnetization loss energy of the layer-wound coil and LNI coil has a little change due to unchanged flux penetration depth in a given power supply current. The contact loss energy of the layer-wound coil and the copper sheet loss energy of the LNI coil decrease with the increase of contact resistivity. However, the contact loss energy of the LNI coil increases rapidly when the contact resistivity increases from 70 to 10000 μΩ cm^2, and then it drops with the increase of contact resistivity. The contact loss energy is related to the contact resistance and the radial current. Higher contact resistivity can lead to less radial current in the coil, which causes the nonmonotonic trend of the contact loss energy. One key result is that the ramping loss energy of the LNI coil is significantly lower than that of the layer-wound coil, even if the two coils have the same contact resistivity.

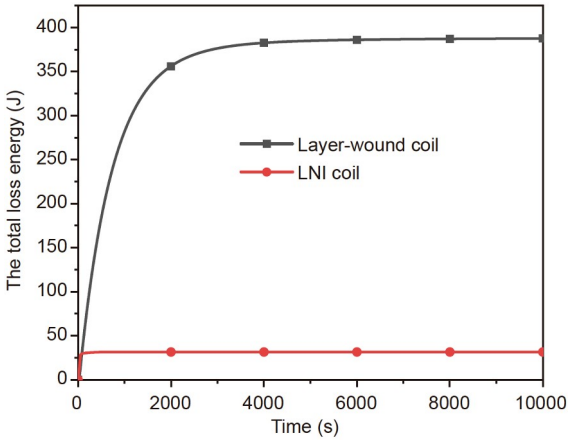

Figure 8 (Color online) The profiles of total ramping loss energy of the layer-wound coil and LNI coil in the ramping process.

Figure 10 shows the effect of different ramping rates of power supply current on the ramping loss energy of the layer-wound coil and LNI coil. The magnetization loss energy of the two coils still has a little change in different ramping rates. The effect of ramping rate of power supply current is not significant on the contact loss of layer-wound coil due to the long charging delay time. However, with the increase of ramping rate, the contact loss and copper sheet loss energy of LNI coil almost have an approximately linear increase. This is because larger radial current and copper sheet current are generated in a larger ramping rate. Namely, the total ramping loss of LNI coil has an obvious increase in a large ramping rate of power supply current.

4 Mechanical characteristics

In this section, the mechanical responses of the layer-wound coil and LNI coil are discussed in the charging process. Compared to the typical layer-wound coil, a copper sheet and a polyimide insulation sheet are inserted into adjacent turns of the LNI coil, which can reduce the charging delay time and ramping loss of the coil. However, the inserted materials may affect the mechanical properties of the LNI coil. Here, a

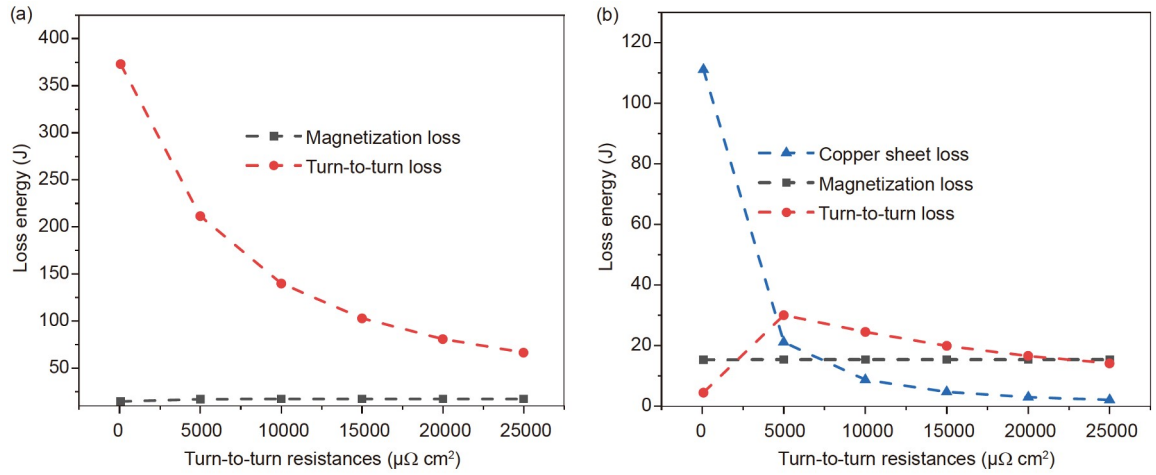

Figure 9 (Color online) The effect of contact resistivities on the ramping loss energy. (a) Layer-wound coil; (b) LNI coil.

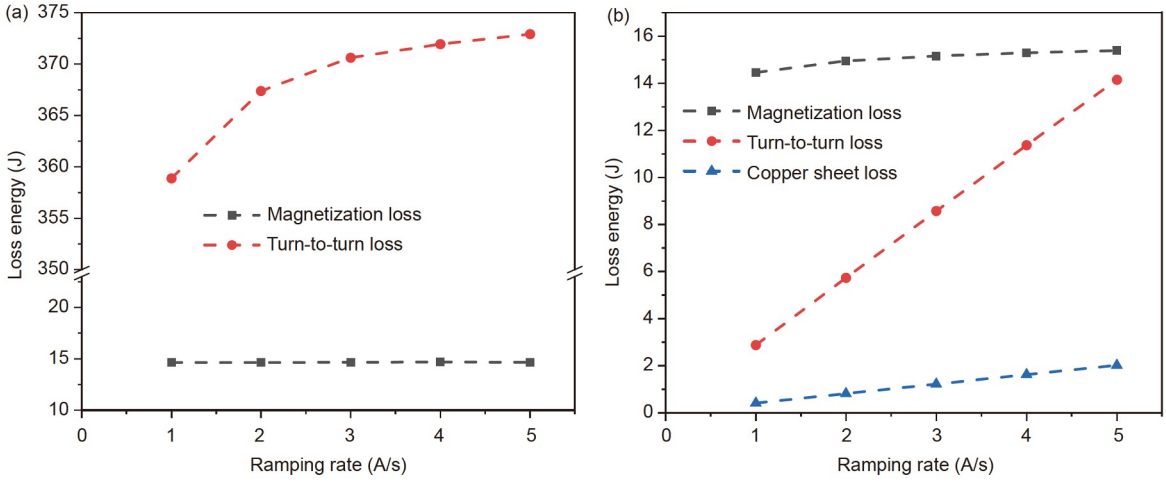

Figure 10 (Color online) The effect of different ramping rates on the ramping loss energy. (a) Layer-wound coil; (b) LNI coil.

15 T background field is applied to the coils. The background field is assumed to be uniform in all computational domains, and the operating current of the coil is 200 A.

4.1 Prestress induced by the cooling process

The superconducting coil usually operates at low temperature, and thus thermal stress is induced by the process of cooling from room temperature to the operating temperature. Figure 11(a) and (b) show the distribution of average hoop stress in each layer of the bottom, middle, and top turns (n_2=1, n_2=5, and n_2=10) of the layer-wound coil and the LNI coil. The hoop stress of the layer-wound coil is small in the cooling process. In the bottom turn of the coil, tensile hoop stress is generated at the inner layers while compressive hoop stress is generated at the outer layers. For the LNI coil, the hoop stress in the REBCO conductor layer has a similar distribution compared to the layer-wound coil; meanwhile, the hoop stress of the polyimide sheet is relatively small and has little change in different layers of the bottom turn of the coil. However, large hoop stress is generated in the copper sheet during the cooling process, where the inner copper sheet experiences maximum hoop stress. This is related to the differences of Young's modulus and thermal expansion coefficient for REBCO conductor, copper sheet, and polyimide sheet. The average hoop stress in the innermost and outermost layers (n_1=1 and n_1=40) of each turn of the layer-wound coil and the LNI coil is shown in Figure 11(c) and (d). It can be found that hoop stress shows a slight difference along the axial direction of the layer-wound coil and LNI coil. Figure 12 shows the averaged axial stress distributions for the layer-wound coil and LNI coil. The axial stress in the REBCO conductor layer of the LNI coil and the layer-wound coil is small in the cooling process. In the LNI coil, the axial

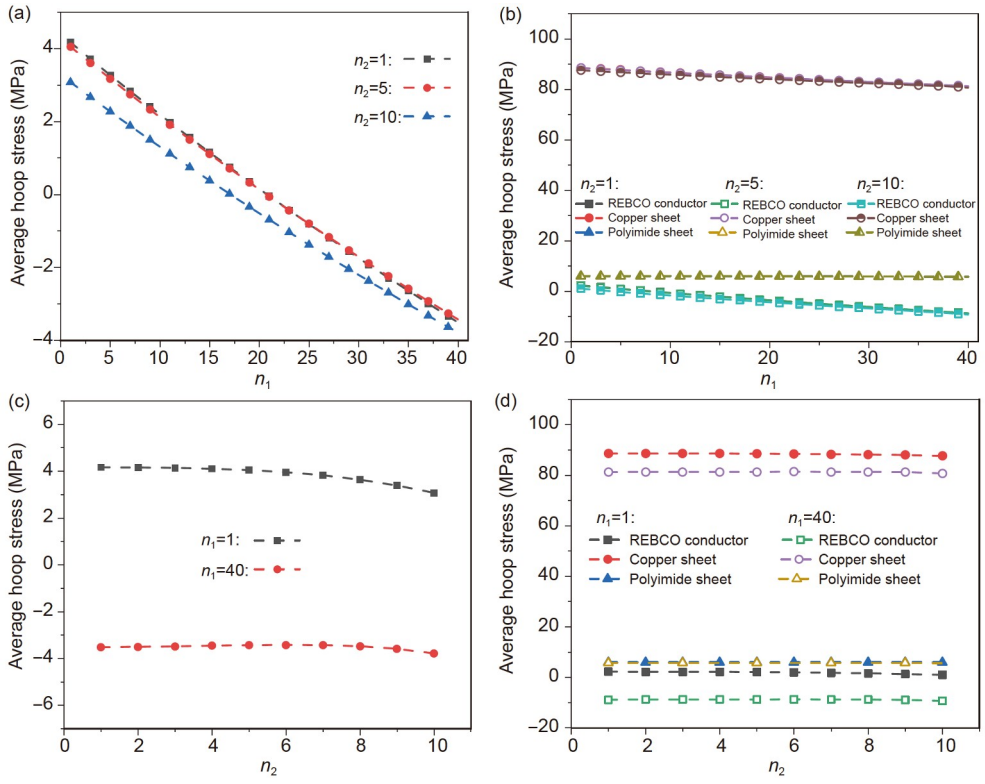

Figure 11 (Color online) Taking into account the cooling process, (a) and (b) are the average hoop stress in each layer of the bottom, middle, and top turns (n_2=1, n_2=5, and n_2=10) of the layer-wound coil and the LNI coil, respectively; (c) and (d) are the average hoop stress in the innermost and outermost layers (n_1=1 and n_1=40) of each turn of the layer-wound coil and the LNI coil, respectively.

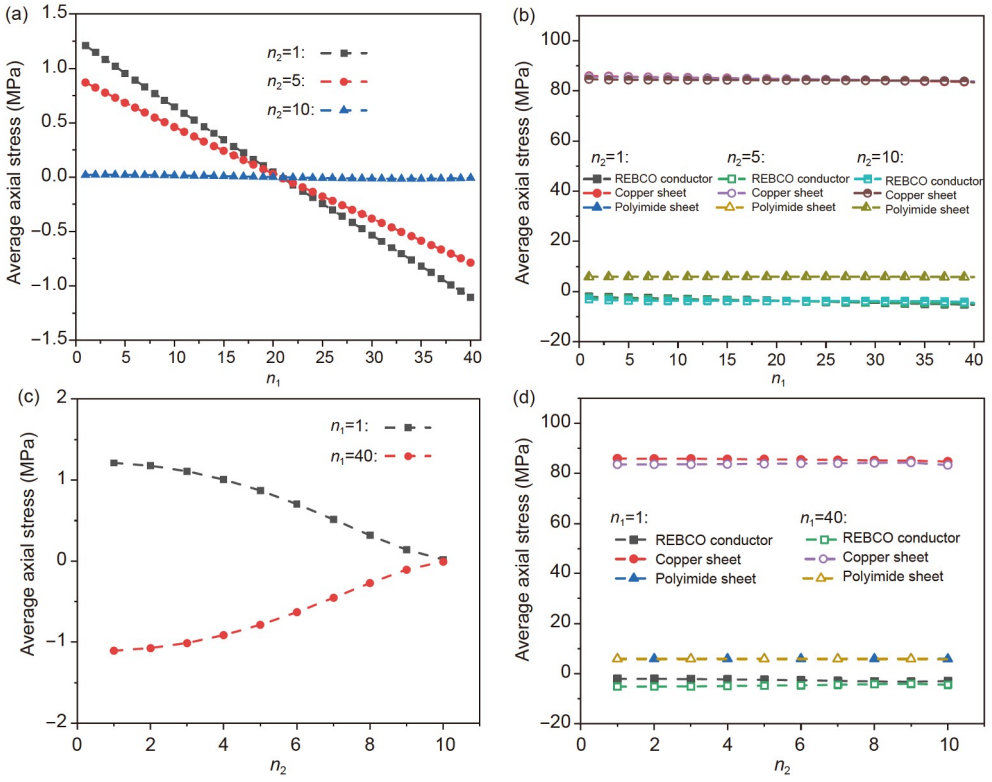

Figure 12 (Color online) Taking into account the cooling process, (a) and (b) are the average axial stress in each layer of the bottom, middle, and top turns (n_2=1, n_2=5, and n_2=10) of the layer-wound coil and the LNI coil, respectively; (c) and (d) are the average axial stress in the innermost and outermost layers (n_1=1 and n_1=40) of each turn of the layer-wound coil and the LNI coil, respectively.

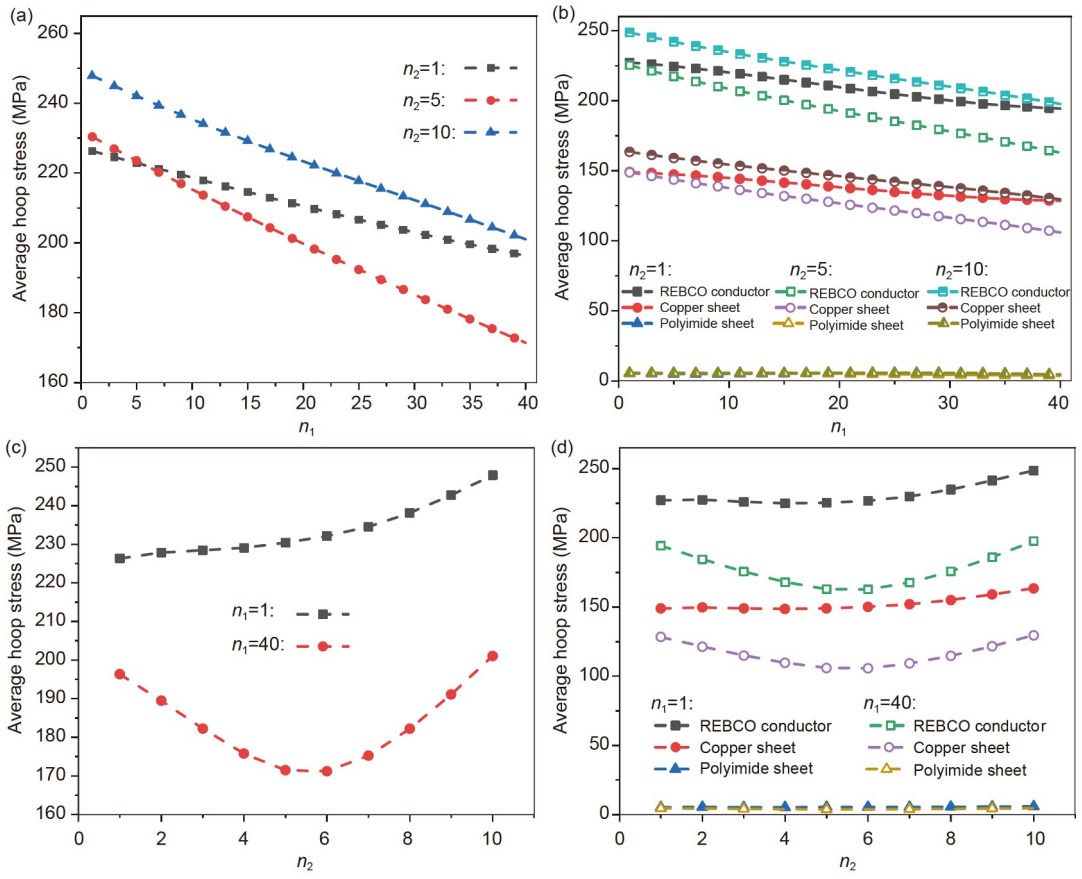

Figure 13 (Color online) In 15 T, only considering the Lorentz force, (a) and (b) are the average hoop stress in each layer of the bottom, middle and top turns (n_2=1, n_2=5, and n_2=10) of the layer-wound coil and the LNI coil, respectively; (c) and (d) are the average hoop stress in the innermost and outermost layers (n_1=1 and n_1=40) of each turn of the layer-wound coil and the LNI coil, respectively.

stress shows slight differences along with the axial and radial directions, and large axial stress is still generated in the copper sheet of the LNI coil. During the cooling process, although the copper sheet of the LNI coil experiences large stress, the stress of the REBCO layer is slightly different from the layer-wound coil.

4.2 Electromagnetic stress induced by Lorentz force

The distributions of electromagnetic stresses induced by Lorentz force in the layer-wound coil and the LNI coil are investigated in this section. Here, we neglect the transient stress during the charging process, and only consider the stress distribution in the steady state. Figure 13(a) and (b) give the change of hoop stress in each layer of the bottom, middle, and top turns (n_2=1, n_2=5, and n_2=10) of the layer-wound coil and the LNI coil. It can be seen that the hoop stress of the REBCO conductor gradually decreases from the inner layers to the outer layers in two coils. Meanwhile, the copper sheet also suffers from large hoop stress in the LNI coil, and the hoop stress in the polyimide sheet is much smaller than other materials. The hoop stress in the innermost and outermost layers (n_1=1 and n_1=40) of each turn of the layer-wound coil and the LNI coil is shown in Figure 13(c) and (d). It can be found that the hoop stress of the REBCO conductor in the innermost layers of two coils increases from the bottom turn to the top turn. However, in the outermost layers of two coils, the turns located in the middle part experience small stress, which is caused by non-uniform mechanical deformation of the coils under the action of electromagnetic force. Moreover, the hoop stress of the copper sheet along the axial direction also has a similar distribution, and the hoop stress of the polyimide sheet is still small.

Figure 14 shows the distribution of axial stress induced by Lorentz force in the layer-wound coil and the LNI coil. In the bottom turn of the coil (n_2=1), compressive axial stress is generated at the inner layers while outer layers experience tensile axial stress. In the middle turn of the coil (n_2=5), the distribution of axial stress has an opposite trend (see Figure 14(a) and (b)). Figure 14(c) and (d) show that the highest axial stress is generated at the middle turn of the coil, while the top and bottom turns have lower axial stresses. In the LNI coil, the axial stress of the REBCO conductor is larger than the copper sheet, and the axial stress of the polyimide sheet is still small. In the case of only taking into

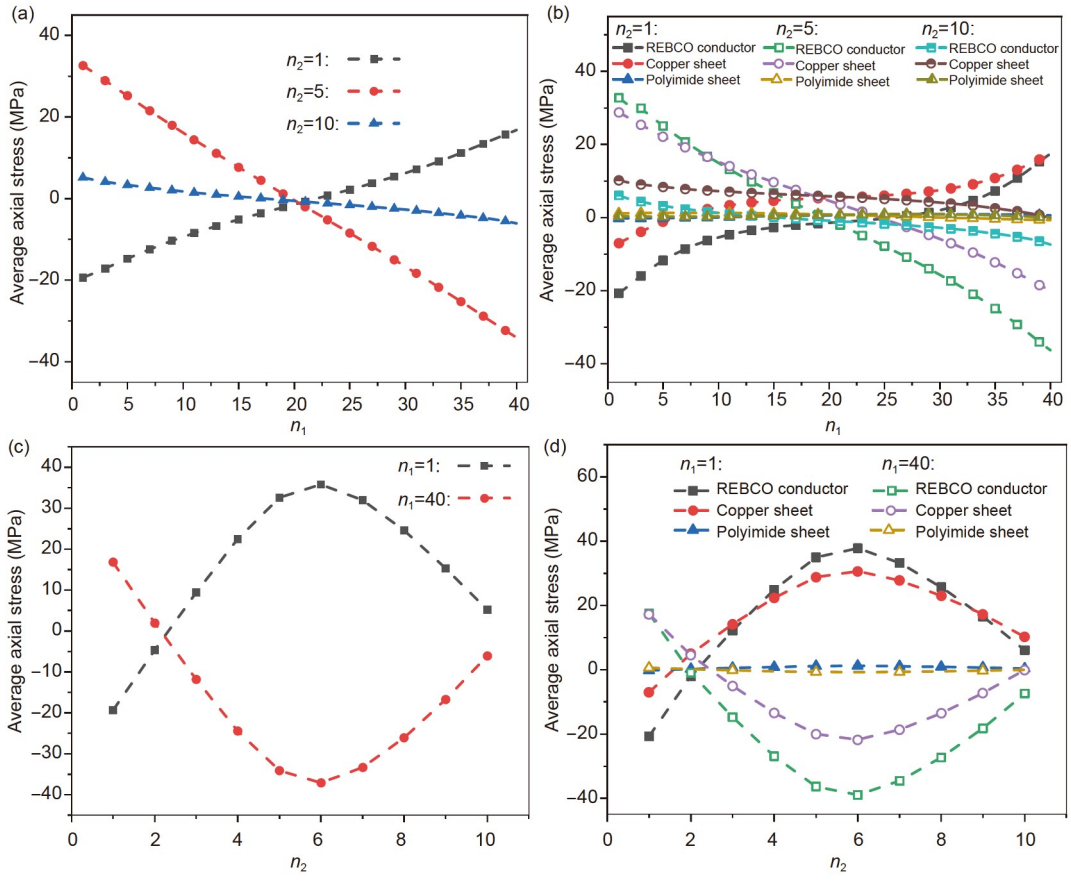

Figure 14 (Color online) In 15 T, only considering the Lorentz force, (a) and (b) are the average axial stress in each layer of the bottom, middle and top turns (n_2=1, n_2=5, and n_2=10) of the layer-wound coil and the LNI coil, respectively; (c) and (d) are the average axial stress in the innermost and outermost layers (n_1=1 and n_1=40) of each turn of the layer-wound coil and the LNI coil, respectively.

account the Lorentz force, the stress distribution in the REBCO conductor of the LNI coil has little difference from that of the layer-wound coil.

4.3 Stress induced by the cooling process and Lorentz force

Here, we take into account the effect of the prestress induced by the cooling process and electromagnetic stress induced by the Lorentz force on the mechanical behaviors of the coil. Figure 15 is the distributions of hoop stress, axial stress, and radial stress of layer-wound coil and LNI coil. In the LNI coil, the copper sheet and the polyimide sheet show different stress states from those of the superconducting layer. Moreover, it can be found that the radial stress of both coils is much smaller than the hoop and axial stresses, so we mainly discuss the hoop and axial stresses.

Figures 16 and 17 show the distributions of the hoop and axial stresses of the coils in this case. It can be seen that the distributions of the hoop and axial stresses are similar to those induced by Lorentz force (see Figures 13 and 14). Namely, the Lorentz force has the main contribution to the mechanical deformation of the coil in the high field. The hoop stress in the top and bottom turns of the coil is asymmetric due to the boundary condition. The hoop stress in the top turn of the coil has a similar trend to that in the bottom turn, while it is slightly higher than the hoop stress in the bottom turn. Moreover, it is worth noting that the stress of the copper sheet is slightly higher than the REBCO conductor in the LNI coil, while the stress of the polyimide sheet is still small by comparing with other materials. In the LNI coil, the maximum stress in the copper sheet is 255 MPa, and the maximum stress in the polyimide sheet is 14 MPa. However, the yield stresses of copper and polyimide can be 340 and 69 MPa, respectively [53,54]. The simulation results show that the LNI winding approach cannot enhance the risk of mechanical damage of the coil under this operating condition.

5 Conclusions

In this paper, we compare the ramping losses and mechanical behaviors of a layer-wound coil and an LNI coil. A hybrid numerical model has been implemented, which combines the equivalent circuit network model with the FEM model.

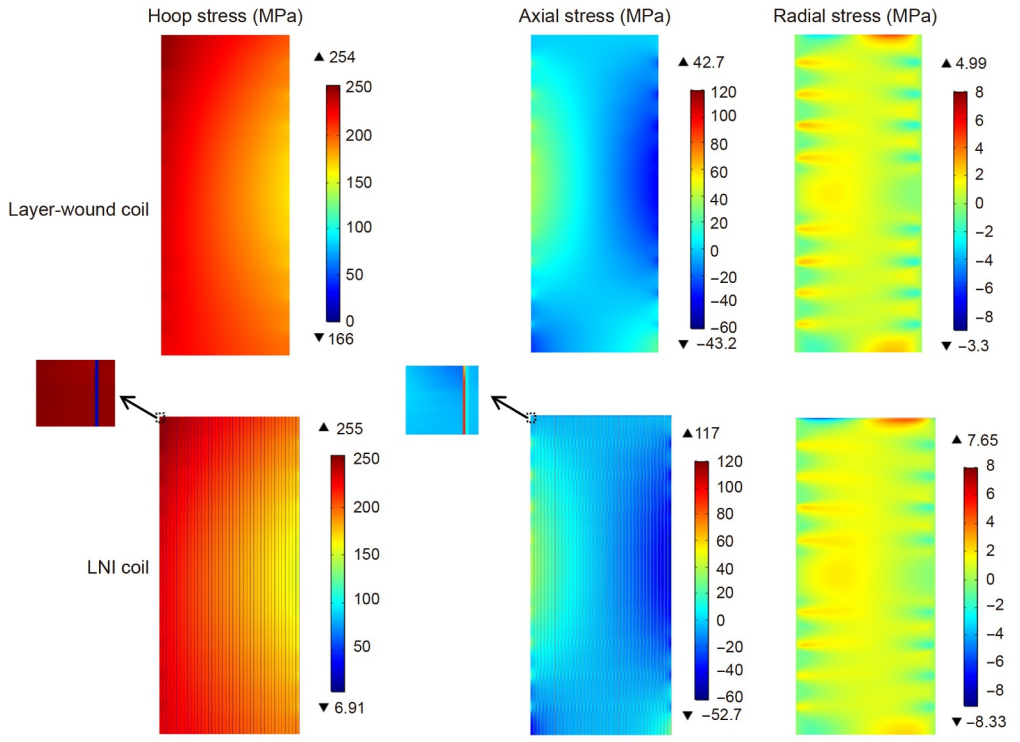

Figure 15 (Color online) The distributions of the hoop stress, axial stress, and radial stress of layer-wound coil and LNI coil. Here, the cooling process and the Lorentz force are taken into account and the background field is 15 T.

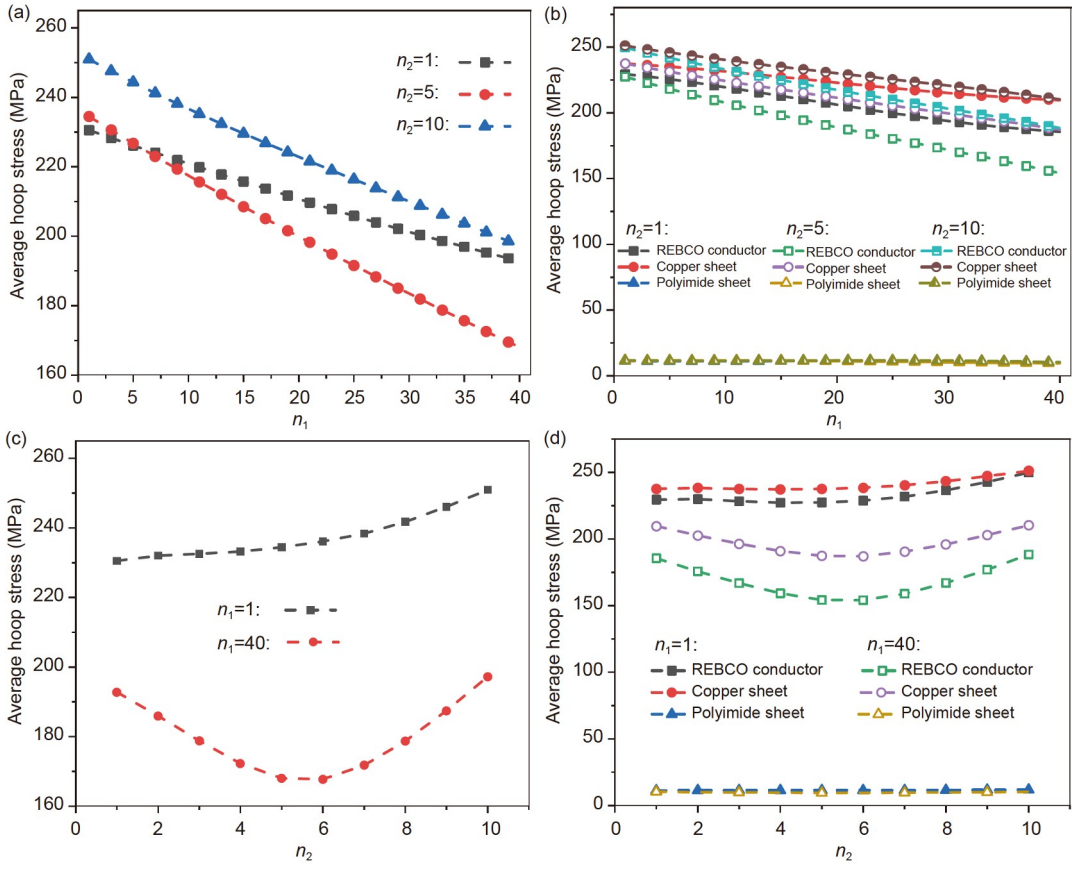

Figure 16 (Color online) In 15 T, taking into account the cooling process and the Lorentz force, (a) and (b) are the average hoop stress in each layer of the bottom, middle and top turns (n_2=1, n_2=5, and n_2=10) of the layer-wound coil and the LNI coil, respectively; (c) and (d) are the average hoop stress in the innermost and outermost layers (n_1=1 and n_1=40) of each turn of the layer-wound coil and the LNI coil, respectively.

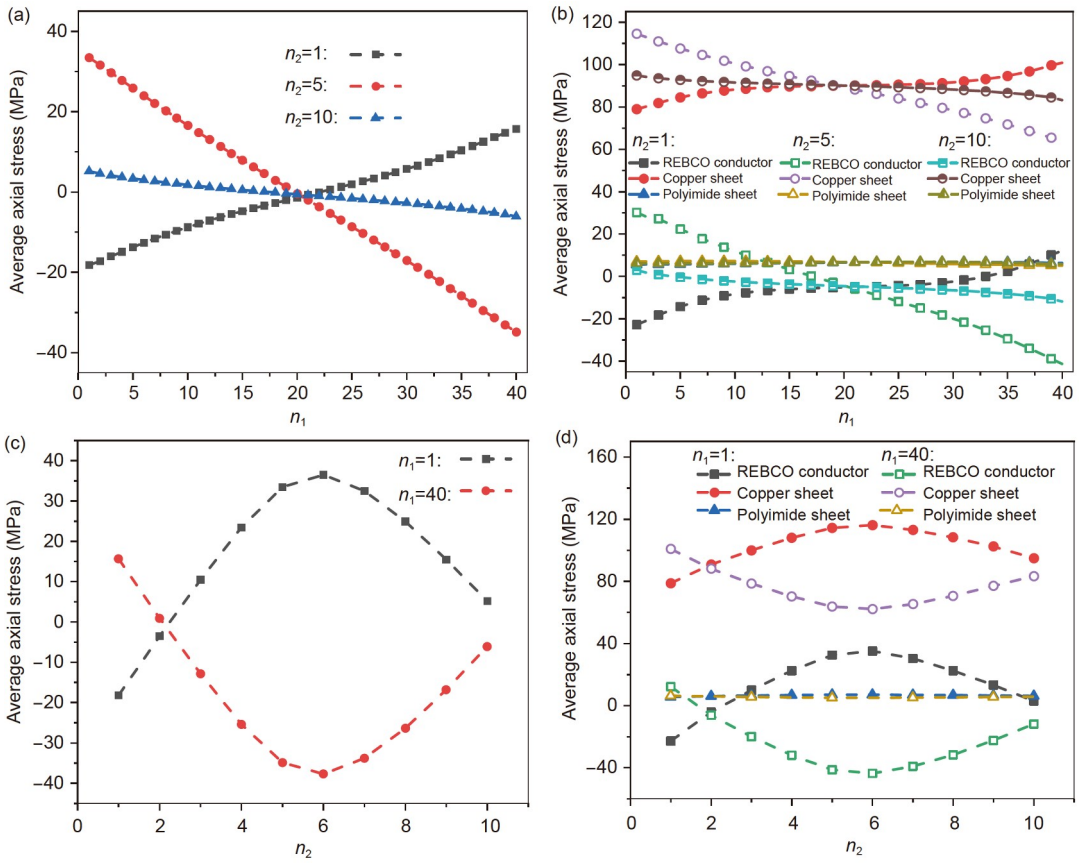

Figure 17 (Color online) In 15 T, taking into account the cooling process and the Lorentz force, (a) and (b) are the average axial stress in each layer of the bottom, middle and top turns (n_2=1, n_2=5, and n_2=10) of the layer-wound coil and the LNI coil, respectively; (c) and (d) are the average axial stress in the innermost and outermost layers (n_1=1 and n_1=40) of each turn of the layer-wound coil and the LNI coil, respectively.

It can be found that the magnetization loss energy of the LNI coil and the layer-wound coil has little difference. However, compared with the layer-wound coil, the LNI coil has a lower contact loss energy due to the shorter charging delay time. The results also indicate that the LNI winding approach can significantly reduce the ramping loss energy in the whole charging process, and thus LNI coil has a higher thermal stability margin. The decrease of the ramping rate of power supply current can significantly reduce the total ramping loss energy of the LNI coil, while its effect on the total ramping loss energy of the layer-wound coil is less obvious. Furthermore, the increase of contact resistivity can significantly reduce the ramping loss of the two coils.

Finally, the distributions of stress in the coils are investigated in three different cases: the cooling process, the Lorentz force, and the combined action of the cooling process and Lorentz force. The hoop stress and axial stress of the REBCO conductor of two coils have a similar distribution in the three cases, and the stress of the polyimide sheet in the LNI coil is small. When considering the cooling process and Lorentz force, it can be found that the Lorentz force has the main contribution to the mechanical deformation of the layer-wound coil and LNI coil in the high field. Meanwhile, the inserted materials have a negligible effect on the hoop stress and axial stress of the LNI coil.

This work was supported by the National Natural Science Foundation of China (Grant Nos. 11872195, 11472120) and the Fundamental Research Funds for the Central Universities (Grant No. lzujbky-2020-1).

1 Hahn S, Park D K, Bascunan J, et al. HTS pancake coils without turn-to-turn insulation. IEEE Trans Appl Supercond, 2011, 21: 1592–1595
2 Yanagisawa Y, Sato K, Yanagisawa K, et al. Basic mechanism of self-healing from thermal runaway for uninsulated REBCO pancake coils. Physica C-Supercond, 2014, 499: 40–44
3 Liu D, Zhang W, Yong H, et al. Thermal stability and mechanical behavior in no-insulation high-temperature superconducting pancake coils. Supercond Sci Technol, 2018, 31: 085010
4 Liu D, Zhang W, Yong H, et al. Numerical analysis of thermal stability and mechanical response in a no-insulation high-temperature superconducting layer-wound coil. Supercond Sci Technol, 2019, 32: 044001
5 Wang Y, Chan W K, Schwartz J. Self-protection mechanisms in no-insulation (RE)$Ba_2Cu_3O_x$ high temperature superconductor pancake coils. Supercond Sci Technol, 2016, 29: 045007
6 Kim K, Kim K, Bhattarai K R, et al. Quench behavior of a no-insulation coil wound with stainless steel cladding REBCO tape at 4.2 K. Supercond Sci Technol, 2017, 30: 075001
7 Quach H L, Kim J H, Hyeon C J, et al. Electrical and thermal analyses of a second generation high temperature superconducting magnet with vanadium III oxide and Kapton polyimide film insulation materials

under an over-pulse current. Supercond Sci Technol, 2019, 32: 065006
8 Song J B, Hahn S, Lécrevisse T, et al. Over-current quench test and self-protecting behavior of a 7 T/78 mm multi-width no-insulation REBCO magnet at 4.2 K. Supercond Sci Technol, 2015, 28: 114001
9 Bhattarai K R, Kim K, Kim S, et al. Quench analysis of a multiwidth no-insulation 7-T 78-mm REBCO magnet. IEEE Trans Appl Supercond, 2017, 27: 4603505
10 Yoon S, Kim J, Cheon K, et al. 26 T 35 mm all-GdBa$_2$Cu$_3$O$_{7-x}$ multi-width no-insulation superconducting magnet. Supercond Sci Technol, 2016, 29: 04LT04
11 Liu D, Li D, Zhang W, et al. Electromagnetic-thermal-mechanical behaviors of a no-insulation double-pancake coil induced by a quench in the self field and the high field. Supercond Sci Technol, 2021, 34: 025014
12 Chan W K, Schwartz J. Improved stability, magnetic field preservation and recovery speed in (RE)Ba$_2$Cu$_3$O$_x$-based no-insulation magnets via a graded-resistance approach. Supercond Sci Technol, 2017, 30: 074007
13 Hahn S, Kim Y, Ling J, et al. No-insulation coil under time-varying condition: Magnetic coupling with external coil. IEEE Trans Appl Supercond, 2013, 23: 4601705
14 Wang Y, Song H. Influence of turn-to-turn resistivity and coil geometrical size on charging characteristics of no-electrical-insulation REBCO pancake coils. Supercond Sci Technol, 2016, 29: 075006
15 Yanagisawa K, Iguchi S, Xu Y, et al. A long charging delay for a no-insulation REBCO layer-wound coil and its influence on operation with outer LTS coils. IEEE Trans Appl Supercond, 2016, 26: 4602304
16 Suetomi Y, Yanagisawa K, Nakagome H, et al. Mechanism of notable difference in the field delay times of no-insulation layer-wound and pancake-wound REBCO coils. Supercond Sci Technol, 2016, 29: 105002
17 Trociewitz U P, Dalban-Canassy M, Hannion M, et al. 35.4 T field generated using a layer-wound superconducting coil made of (RE)Ba$_2$Cu$_3$O$_{7-x}$ (RE=rare earth) coated conductor. Appl Phys Lett, 2011, 99: 202506
18 Matsumoto S, Kiyoshi T, Otsuka A, et al. Generation of 24 T at 4.2 K using a layer-wound GdBCO insert coil with Nb$_3$Sn and Nb-Ti external magnetic field coils. Supercond Sci Technol, 2012, 25: 025017
19 Matsumoto S, Choi S, Kiyoshi T, et al. REBCO layer-wound coil tests under electromagnetic forces in an external magnetic field of up to 17.2 T. IEEE Trans Appl Supercond, 2012, 22: 9501604
20 Suetomi Y, Takahashi S, Takao T, et al. A novel winding method for a no-insulation layer-wound REBCO coil to provide a short magnetic field delay and self-protect characteristics. Supercond Sci Technol, 2019, 32: 045003
21 Yoshida T, Suetomi Y, Takahashi K, et al. Performance of epoxy-impregnated intra-layer no-insulation (LNI) REBCO coils at 77 K. IEEE Trans Appl Supercond, 2021, doi: 10.1109/TASC.2021.3065875
22 Suetomi Y, Yoshida T, Takahashi S, et al. Quench and self-protecting behaviour of an intra-layer no-insulation (LNI) REBCO coil at 31.4 T. Supercond Sci Technol, 2021, 34: 064003
23 Grilli F, Ashworth S P. Measuring transport AC losses in YBCO-coated conductor coils. Supercond Sci Technol, 2007, 20: 794–799
24 Zhang M, Yuan W, Kvitkovic J, et al. Total AC loss study of 2G HTS coils for fully HTS machine applications. Supercond Sci Technol, 2015, 28: 115011
25 Ryu K, Choi B J, Chun Y H. Magnetization loss characteristics in a stack of Bi-2223 tapes. IEEE Trans Appl Supercond, 2003, 13: 2360–2363
26 Escamez G, Badel A, Tixador P, et al. Numerical modelling of AC hysteresis losses in HTS tubes. IEEE Trans Appl Supercond, 2015, 25: 8201505
27 Niu M, Yong H, Xia J, et al. The effects of ferromagnetic disks on AC losses in HTS pancake coils with nonmagnetic and magnetic substrates. J Supercond Nov Magn, 2019, 32: 499–510
28 Wang Y, Song H, Yuan W, et al. Ramping turn-to-turn loss and magnetization loss of a No-Insulation (RE)Ba$_2$Cu$_3$O$_x$ high temperature superconductor pancake coil. J Appl Phys, 2017, 121: 113903
29 Ang Z, Bejar I, Bottura L, et al. Measurement of AC loss and magnetic field during ramps in the LHC model dipoles. IEEE Trans Appl Supercond, 1999, 9: 742–745
30 Jang J Y, Yoon S, Hahn S, et al. Design, construction and 13 K conduction-cooled operation of a 3 T 100 mm stainless steel cladding all-REBCO magnet. Supercond Sci Technol, 2017, 30: 105012
31 Mbam S O, Gou X F. Interface crack growth rate and fatigue life of multilayer-coated conductor tapes. Eng Fract Mech, 2020, 228: 106910
32 Wang T, Li Z, Cao J, et al. Mechanical damage of YBa$_2$CU$_3$O$_7$-coated conducting film caused by its CeO$_2$ interface with defects. Int J Appl Mech, 2019, 11: 1950038
33 Zhang X, Sun C, Liu C, et al. A standardized measurement method and data analysis for the delamination strengths of YBCO coated conductors. Supercond Sci Technol, 2020, 33: 035005
34 Gao P, Chan W K, Wang X, et al. Mixed-dimensional modeling of delamination in rare earth-barium-copper-oxide coated conductors composed of laminated high-aspect-ratio thin films. Supercond Sci Technol, 2018, 31: 074004
35 Lécrevisse T, Badel A, Benkel T, et al. Metal-as-insulation variant of no-insulation HTS winding technique: Pancake tests under high background magnetic field and high current at 4.2 K. Supercond Sci Technol, 2018, 31: 055008
36 Shin H S, Dedicatoria M J. Variation of the strain effect on the critical current due to external lamination in REBCO coated conductors. Supercond Sci Technol, 2012, 25: 054013
37 Su X, Liu C, Zhou J, et al. A method to access the electro-mechanical properties of superconducting thin film under uniaxial compression. Acta Mech Sin, 2020, 36: 1046–1050
38 Liu J, Wang Q, Qin L, et al. World record 32.35 tesla direct-current magnetic field generated with an all-superconducting magnet. Supercond Sci Technol, 2020, 33: 03LT01
39 Bhattarai K R, Kim K, Kim K, et al. Understanding quench in no-insulation (NI) REBCO magnets through experiments and simulations. Supercond Sci Technol, 2020, 33: 035002
40 Wang Y, Zhang M, Yuan W, et al. Non-uniform ramping losses and thermal optimization with turn-to-turn resistivity grading in a (RE)Ba$_2$Cu$_3$O$_x$ magnet consisting of multiple no-insulation pancake coils. J Appl Phys, 2017, 122: 053902
41 Wang X, Hahn S, Kim Y, et al. Turn-to-turn contact characteristics for an equivalent circuit model of no-insulation ReBCO pancake coil. Supercond Sci Technol, 2013, 26: 035012
42 Liu D, Yong H, Zhou Y. Analysis of charging and sudden-discharging characteristics of no-insulation REBCO coil using an electromagnetic coupling model. AIP Adv, 2017, 7: 115104
43 Wang T, Noguchi S, Wang X, et al. Analyses of transient behaviors of no-insulation REBCO pancake coils during sudden discharging and overcurrent. IEEE Trans Appl Supercond, 2015, 25: 4603409
44 Rhyner J. Magnetic properties and AC-losses of superconductors with power law current-voltage characteristics. Physica C-Supercond, 1993, 212: 292–300
45 Grilli F, Sirois F, Zermeno V M R, et al. Self-consistent modeling of the I_c of HTS devices: How accurate do models really need to be? IEEE Trans Appl Supercond, 2014, 24: 8000508
46 Liang F, Venuturumilli S, Zhang H, et al. A finite element model for simulating second generation high temperature superconducting coils/stacks with large number of turns. J Appl Phys, 2017, 122: 043903
47 Zhang H, Zhang M, Yuan W. An efficient 3D finite element method model based on the T-A formulation for superconducting coated conductors. Supercond Sci Technol, 2017, 30: 024005
48 Noguchi S. Electromagnetic, thermal, and mechanical quench simulation of NI REBCO pancake coils for high magnetic field generation. IEEE Trans Appl Supercond, 2019, 29: 4602607
49 Xia J, Bai H, Yong H, et al. Stress and strain analysis of a REBCO high field coil based on the distribution of shielding current. Supercond Sci Technol, 2019, 32: 095005

50 Gao P, Wei X, Wu B, et al. Numerical investigation on decreasing radial stress in epoxy impregnated REBCO pancake coils by overband. Cryogenics, 2019, 103: 102971
51 Niu M, Xia J, Yong H, et al. Quench characteristics and mechanical responses during quench propagation in rare earth barium copper oxide pancake coils. Appl Math Mech-Engl Ed, 2021, 42: 235–250
52 Boso D P. A simple and effective approach for thermo-mechanical modelling of composite superconducting wires. Supercond Sci Technol, 2013, 26: 045006
53 Zhang Y, Hazelton D W, Kelley R, et al. Stress-strain relationship, critical strain (stress) and irreversible strain (stress) of IBAD-MOCVD-based 2G HTS wires under uniaxial tension. IEEE Trans Appl Supercond, 2016, 26: 8400406
54 DUPONT Kapton® HN general-purpose polyimide film. https://www.dupont.com/products/kapton-hn.html
55 Osamura K, Sugano M, Machiya S, et al. Internal residual strain and critical current maximum of a surrounded Cu stabilized YBCO coated conductor. Supercond Sci Technol, 2009, 22: 065001
56 Dizon J R C, Nisay A R N, Dedicatoria M J A, et al. Analysis of thermal residual stress/strain in REBCO coated conductor tapes. IEEE Trans Appl Supercond, 2014, 24: 8400905
57 Ilin K, Yagotintsev K A, Zhou C, et al. Experiments and FE modeling of stress-strain state in ReBCO tape under tensile, torsional and transverse load. Supercond Sci Technol, 2015, 28: 055006
58 Hsueh C H, Paranthaman M. Analytical modeling of residual stresses in multilayered superconductor systems. J Mater Sci, 2008, 43: 6223–6232
59 Ochiai S, Rokkaku H, Morishita K, et al. Thermally induced residual strain accumulation in Bi2223/Ag/Ag alloy composite superconductor. Supercond Sci Technol, 2007, 20: 202–210
60 Zhang Z, Chen W, Gou X. Numerical studies of thermally induced residual strain/stress in $Bi_2Sr_2Ca_2Cu_3O_x$/Ag/Ag alloy composite tapes and the dependence of material properties on the temperature. J Supercond Nov Magn, 2014, 27: 1387–1396
61 Cheon J H, Shankar P S, Singh J P. Influence of processing methods on residual stress evolution in coated conductors. Supercond Sci Technol, 2004, 18: 142–146
62 Miyagi D, Kato M, Yoshida Y, et al. Influence of a coil bobbin on transient thermal stress in a REBCO pancake coil. IEEE Trans Appl Supercond, 2018, 28: 4603505